JOURNAL OF GUIDANCE, CONTROL, AND DYNAMICS
Vol. 38, No. 9, September 2015

Spacecraft Navigation Using Celestial Gamma-Ray Sources

Chuck S. Hisamoto* and Suneel I. Sheikh†
ASTER Labs, Inc., Shoreview, Minnesota 55126

DOI: 10.2514/1.G001008

As the future progresses for space exploration endeavors, spacecraft that are capable of autonomously determining their position and velocity will provide clear navigation advances to mission operations. Thus, new techniques for determining spacecraft navigation solutions using celestial gamma-ray sources have been developed. Most of these sources offer detectable, bright, high-energy events that provide well-defined characteristics conducive to accurate time alignment among spatially separated spacecraft. Using assemblages of photons from distant gamma-ray bursts, relative range between two spacecraft can be accurately computed along the direction to each burst's source based upon the difference in arrival time of the burst emission at each spacecraft's location. Correlation methods used to time-align the high-energy burst profiles are provided. A simulation of the newly devised navigation algorithms has been developed to assess the system's potential performance. Using predicted observation capabilities for this system, the analysis demonstrates position uncertainties comparable to the NASA Deep Space Network for deep-space trajectories.

Nomenclature

c	=	speed of light, m/s
$\boldsymbol{f}$	=	nonlinear state vector function
$\boldsymbol{h}$	=	nonlinear simulated state vector function
H	=	measurement matrix of partial derivatives with respect to states
$\{i, j, k\}$	=	spacecraft coordinate system unit axis directions
$\hat{n}$	=	line-of-sight vector, radians
r_{SC}	=	three-dimensional spacecraft position, m
r_{Base}	=	three-dimensional base station position, m
S	=	fluence, $\text{erg}/\text{cm}^2/T_{90}$
t_0	=	emission trigger time, s
T_{90}	=	burst emission time from 5 to 95% of total photon counts, s
$\boldsymbol{\nu}$	=	simulated measurement noise vector
$\boldsymbol{v}_{\text{RSC}}$	=	remote spacecraft velocity, m/s
$\boldsymbol{x}$	=	extended Kalman filter (EKF) true state vector
$\dot{x}(t)$	=	nonlinear spacecraft orbital dynamics
$\tilde{\boldsymbol{x}}$	=	EKF estimated state vector
y	=	observation (filter measurement)
z	=	EKF measurement difference
$z(t)$	=	measurement residual
Δr	=	burst position offset, m
Δt	=	burst arrival time offset, s
$\boldsymbol{\delta x}$	=	state vector errors
$\boldsymbol{\eta}(t)$	=	measurement noise vector
σ_{pos_0}	=	EKF initial position covariance estimate, m
σ_{vel_0}	=	EKF initial velocity covariance estimate, m/s

I. Introduction

FOR space vehicles venturing beyond Earth orbit into deep space, current navigation methods require frequent interaction and communication with Earth stations, which can significantly increase mission scheduling and operational costs. The NASA Deep Space Network (DSN) is the primary provider of navigation and communication for the United States and its partnering nations on deep-space missions [1,2]. DSN's capability has achieved mission success throughout its over 50 years of operation. However, as exploration initiatives increase and operational usage expands, the DSN has the potential for oversubscription due to its many ongoing and future planned missions, and thus stands to benefit from supplemental navigation augmentation capabilities designed to reduce DSN operations cost. In addition to improved operational support, expanded exploration of our solar system beyond current day capabilities will require innovative, nonconventional techniques for vehicle navigation. Very few existing systems can provide this additional service while reducing DSN workload. Therefore, new methods are required that support the DSN system by alleviating any operational interruptions and providing for increased operational autonomy of deep-space vehicles.

To address the challenges of future DSN operation and enhance position accuracy for deep-space vehicles, a novel relative navigation technology for deep-space exploration using measurements of celestial gamma-ray sources has been developed that incorporates existing designs of autonomous navigation technologies and merges these with the developing science of high-energy sensor components. This new technology for interplanetary self-navigation, referred to as gamma-ray source localization-induced navigation and timing (GLINT), provides important enhancements to planned exploration and discovery missions, specifically by increasing the onboard navigation and guidance capabilities, thereby reducing operational risk.

Previous studies of a navigation system based on variable celestial x-ray sources (0.1–20 keV), referred to as the x-ray navigation and autonomous position verification program (XNAV), has shown the capability to support DSN measurements for deep-space missions [3–9]. The analysis of the unique and periodic nature of x-ray pulsar sources used in this past study provides a basis for the new GLINT navigation concept. XNAV relies on pulsars located at known positions on the sky and a pulse-timing model of the expected arrival time of each pulse. The periodic nature of these pulsar sources provides a reliable signal that can be continually detected and tracked. An XNAV range measurement is calculated using an observed pulse profile on a spacecraft and the predicted pulse arrival time from each pulsar's model. The observation time required to produce an individual XNAV measurement depends on each pulsar's unique characteristics and the spacecraft's detector qualities. Although there are a number of well-distributed pulsars along the celestial sphere, many x-ray pulsars are faint and require long observation times to generate sufficient usable data [7].

This new GLINT concept extends the XNAV navigation elements to use celestial sources emitting much higher-energy photons (20 keV–1 MeV). Although there are several types of celestial

Presented at the 23rd AAS/AIAA Space Flight Mechanics Meeting, Kauai, HI, 10–14 February 2013; received 27 August 2014; revision received 12 September 2014; accepted for publication 8 January 2015; published online 8 April 2015.

*Research Scientist, ASTER Labs, Inc., 155 East Owasso Lane. Member AIAA.

†Chief Research Scientist, ASTER Labs, Inc., 155 East Owasso Lane. Senior Member AIAA.

sources that emit γ-rays, this paper details GLINT techniques to use γ-ray photons from distant celestial gamma-ray bursts (GRBs) to provide measurements supporting the continual estimation of three-dimensional (3-D) spacecraft position and velocity. Whereas XNAV concepts can compute an absolute position of a spacecraft with respect to an inertial origin, the overall GLINT concept measures the relative range of an observing vehicle with respect to a reference observer along the line of sight (LOS) to a celestial source. This relative position is computed using multiple relative-range measurements based upon the difference in the arrival time of the burst at each spacecraft's location. These relative-range measurements can be computed anywhere in the solar system (and beyond), wherever a spacecraft and reference station can detect the same burst and share their reception information. Although these bursting events are aperiodic, happening only once per star, GRBs emanate from all directions of the sky with sufficient regularity for navigation. GLINT-based navigation solutions can be continuously updated while on an interplanetary cruise or in orbit about a destination planetary body, including asteroids. As a relative navigation solution, GLINT is intended to complement the existing DSN infrastructure, and the eventual XNAV implementations.

A significant advantage supporting the GLINT implementation is that γ-ray detectors are currently incorporated on almost all deep-space missions and science missions in Earth orbit as part of their instrument package. These detectors support the science investigations of space radiation, as well as evaluation of the composition of elements on planetary bodies. Several operating γ-ray detection systems are continuing to actively collect GRB photon data, providing an ongoing resource for GLINT analysis. Although GRB sources are nonrepeating and nonperiodic due to their cataclysmic nature, their flux intensities are much higher than most other high-energy celestial sources, including x-ray pulsars studied previously [5,6]. GRBs therefore yield higher signal-to-noise and more well-defined morphological profile characteristics for burst time comparisons.

An initial study using past and current observed γ-ray mission data has demonstrated that the relative navigation performance of tens to hundreds of kilometers accuracy is readily available. However, it will be shown that subkilometer level positioning is expected to be achieved by the GLINT system using enhanced photon timing and processing algorithms.

II. Celestial Gamma-Ray Sources

GRBs are the most powerful explosions known in the universe [10]. They are extremely luminous, with many orders of magnitude more energy output in a few seconds than our sun emits in a year. GRBs are theorized to be produced during the evolutionary end-stages of single and binary star systems. This includes the unusually energetic supernova explosions (so-called hypernovas), the merger of two neutron stars, or when a small star is consumed by a black hole [11].

GRBs have been detected approximately once per day by past and existing science missions, although they are theorized to occur at a much higher rate due to the concept of *beaming*, in which the emissions from a burst are focused into only one-one hundredth of the total sky [12]. Thousands of GRBs have been detected since they were initially discovered in 1967 by the Vela satellites [13]. GRB events are typically named and catalogued according to their detection date, in the format GRBYYYYMMDDx, where x is an optional letter designation for cases in which multiple bursts occur on a given day. These sources are typically detectable via their emissions in the tens of keV to MeV, and often higher, photon energy bands. Figure 1 shows a rendering of a GRB after the collapse and explosion of the star, at which time energy is jettisoned from the core of the burst [14].

Other sources include γ-ray pulsars, which exhibit highly predictable timing behavior, potentially enabling applications that rely on the regularity of their pulsations [15]. However, the very low photon flux rates (typically $<10^{-7}$ ph/cm^2/s, several orders of magnitude lower than x-ray pulsar fluxes) of these sources make their use an extreme challenge for a practical navigation system, requiring a large detector area [7]. Therefore for spacecraft navigation, the more practical γ-ray sources are those of the high-flux GRB type.

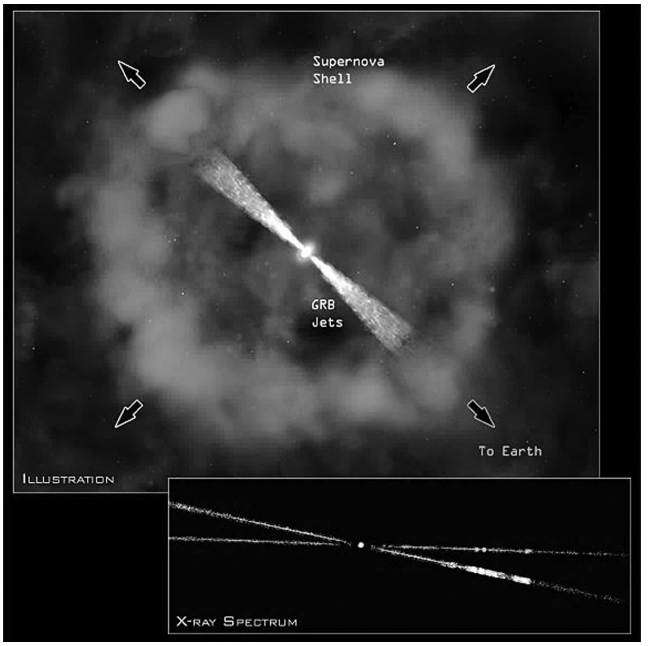

Fig. 1 An artistic rendition of a GRB and its components. (From Sazonov et al. [14]; Credit: Illustration: CXC/M. Weiss; Spectrum: NASA/CXC/N.)

III. GRB Source Classification and Characterization

GRBs are typically classified morphologically into a few distinct classes, based on temporal and flux characteristics [16–19]. Using the term T_{90} as the time over which the burst emits from 5 to 95% of its total photon counts, long bursts are those with $T_{90} > 2$ s, and are thought to be related to massive star collapse [19]. Short bursts, likewise, exhibit a duration of $T_{90} < 2$ s. Another classification approach is fluence, S, which is the photon flux integrated over time. High-fluence bursts exhibit $S > 1.6 \times 10^{-4}$ erg/cm$^2/T_{90}$, whereas low-fluence bursts are those with $S < 1.6 \times 10^{-4}$ erg/cm$^2/T_{90}$. Most bursts exhibit some degree of a fast rise and exponential decay (FRED) behavior.

Short bursts are known to have harder spectra than long bursts, where a greater proportion of the detected photons are of higher energy [20]. The importance of spectral properties, coupled with the sensitive energy band, E, of a given detector, can be seen in the relative statistics of GRB detection between instruments and missions. For example, the Fermi spacecraft's gamma-ray burst monitor (GBM), with an effective area a factor of ~3 smaller than that of Swift's Burst Alert Telescope (BAT), detects 1.5 times more GRBs per year [21]. The reason for this dramatic difference is, in part, GBM's greater sky coverage, but also that GBM's sensitivity extends over a much broader energy band (8 keV $\leq E \leq$ 30 MeV) than does BAT (15 keV $\leq E \leq$ 150 keV) [22]. Because the GBM's higher-energy response is a better match to the hard-spectrum emission from short bursts, a significantly larger fraction of bursts detected by GBM are short, compared to BAT. Because short bursts tend to contain narrower temporal features that are better suited to high-precision time of arrival comparison, the hard-spectrum nature of these types of bursts may dictate future GLINT detector design decisions for optimized performance. Figure 2 provides four unique GRB profiles recorded by various detector missions, which illustrate the diversity of burst characteristics. In each subplot, the solid and dashed signals represent the incoming fluxes as received by the respective spacecraft's detector. Differences in flux magnitude between two observing spacecraft, which can vary dramatically as shown, are due to the different detector properties on each spacecraft.

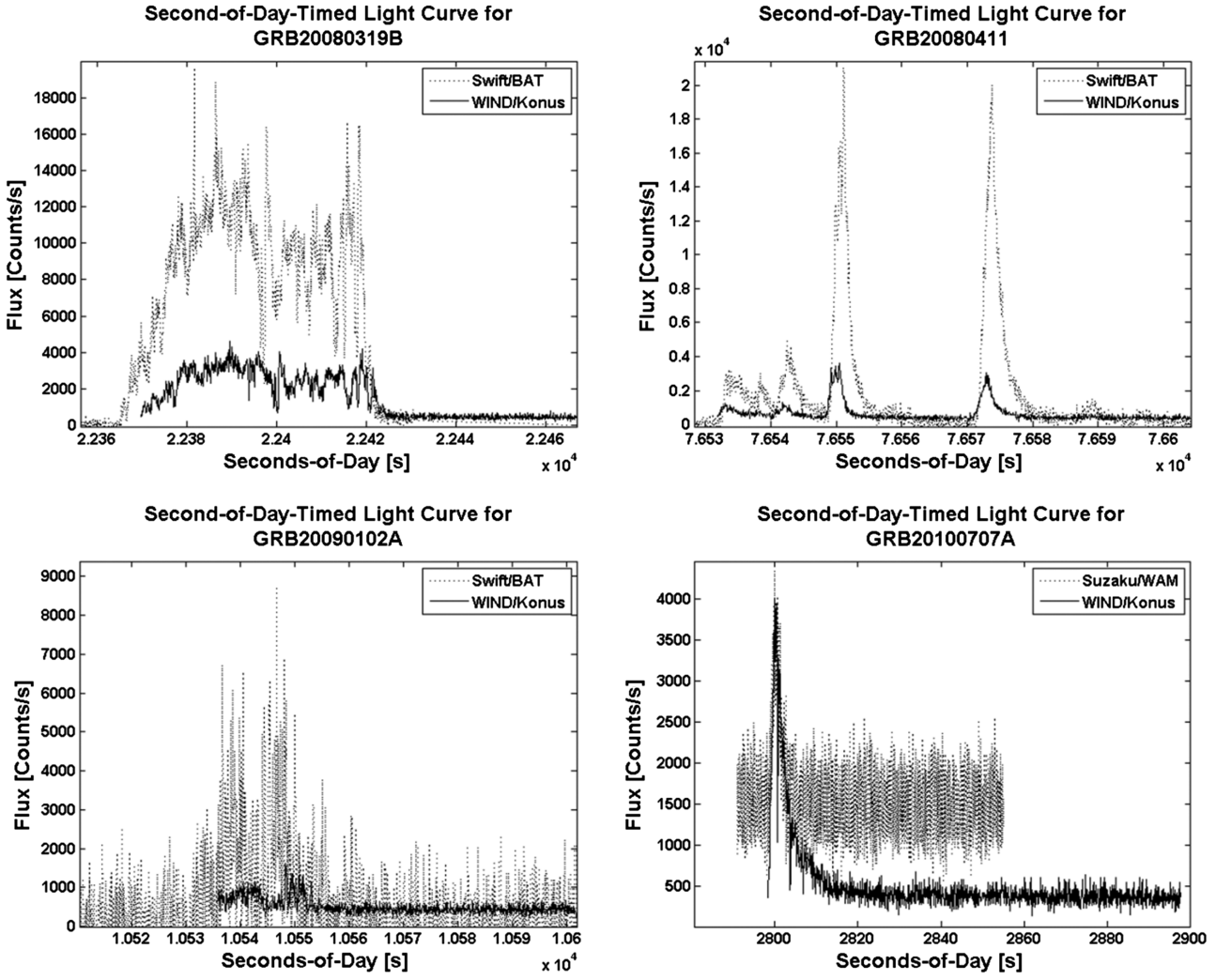

Fig. 2 Sample of burst profiles for selected GLINT-processed GRBs.

IV. Interplanetary Network and GRB Coordinates Network

A significant Earth-based infrastructure has been built to observe GRBs and rapidly disseminate information about their occurrence and localizations. The Interplanetary Network (IPN), in existence for over 30 years, comprises an inhomogeneous collection of in-space monitoring platforms that triangulate the position of a GRB from the burst arrival time differences between spacecraft [23]. This source localization service by IPN spacecraft provides an architecture for GRB timing and positioning.

The GRB Coordinates Network (GCN), established by NASA's Goddard Space Flight Center, gathers input from IPN and optical and radio ground stations to disseminate the position of a GRB to observers as quickly as possible, sometimes less than a minute after detection. This existing GRB observational infrastructure of supporting spacecraft and Earth observation systems provides a preliminary basis for the architecture of the operational GLINT system. The network of IPN vehicles, many with ongoing and extended missions, along with future planned missions already being equipped with γ-ray detectors capable of high-accuracy timing, ensures the data availability and source identification and localization that feed the GLINT concept.

Historically, detections by many geometrically distributed observers of the afterglow of a GRB subsequent to its detection have provided localization of the GRB on the sky. The accurate position knowledge of each observer assisted with the localization. Today, the Swift mission, with its GRB detector plane area of $\sim$5200 cm^2, localizes GRBs at the arcsecond level, and ground- or space-based follow-up in the optical or radio bands can localize afterglows to significantly better than an arcsecond of accuracy.

V. GLINT Navigation System Architecture

This multispacecraft localization process, as part of the GCN and IPN, improves the analysis of these one-time celestial GRB events. In principle, however, the IPN procedure can be inverted to improve or determine independently the position of any spacecraft that detects a GRB that has been well localized. This is the basic concept of GLINT, detailed in Fig. 3. The primary elements of a notional GLINT system architecture include a base observational reference station orbiting Earth, and a remote space vehicle. Both the base and remote spacecraft detect the same GRB event. Earth ground station data

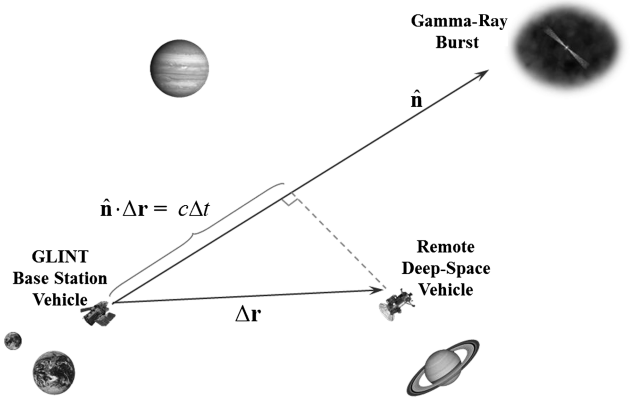

Fig. 3 Observations of GRB event by GLINT base station and remote spacecraft.

processing is used to support the rapid dissemination of GRB data products among cooperating vehicles.

The computation of a range measurement between a GLINT base and remote spacecraft when each observe a GRB proceeds as follows. High-efficiency γ-ray photon detectors onboard the base and remote spacecraft would accumulate a light curve for the duration of the GRB using fine-resolution time-tagged photon arrival times to ensure precise and accurate observations. The accurate LOS to a GRB, $\hat{n}$, is disseminated by the IPN/GCN system once the GRB has been precisely localized. To provide the required GRB localization accuracy, the GLINT base station would require Swift-like arcsecond localization capabilities, or incorporate optical follow-up information from ground or space assets. The GLINT-equipped remote spacecraft would use the base station's template light curve profile and its own observed data, along with the known accurate sky position disseminated by the IPN/GCN, to compute the time difference of arrival (TDOA) of the GRB between spacecraft. Using this measured burst TDOA, the remote spacecraft would compute its position relative to the base station and a navigation solution incorporating this measured relative distance would be updated, providing a refined navigation solution.

Two potential data transmission and processing paths are available for GLINT.

1) In one approach, the processing of the TDOA between the acquired light curves and the relative navigation solution, including any cross-correlation and filtering techniques, would be performed onboard the GLINT-equipped spacecraft and its navigation solution would be directly updated. Thus, the data telemetry path is *up* to the remote spacecraft, where the remote vehicle itself computes and updates its own navigation solution to autonomously operate through its mission or report its known location to mission control when requested.

2) In another approach, the light curves obtained by each observing spacecraft would be telemetered down to a central ground- or space-based processing station. The cross correlation between light curves and navigation solution refinement would be performed at this central station. The updated navigation solution based on the relative distances would then be maintained at the central station and future control maneuvers could be planned accordingly based upon that navigation solution.

VI. GRB Photon Data Processing

Observational data of a GRB primarily include the time of the detected event, its location, and a binned table of photon count data over a specified time interval. These light curve data files provide the shape and intensity of a single GRB. Among the primary components of the light curve files found in public databases or obtained by permission of the mission scientists is a trigger time, which specifies a starting time, t_0, for the emission event, individual bin time stamps, total photon counts in each time bin, and energy range of binned photons. This data set can be compared between mutually observing spacecraft to improve knowledge of the relative positions of the spacecraft by correlating the difference of the time of arrival between detections. The time offset, Δt, of the burst arrival time at two spacecraft is related to their position offset, Δr, along the unit LOS to the GRB, $\hat{n}$, as the following, where superscript T denotes the vector transpose

$$\hat{n}^T \Delta r = c\Delta t \tag{1}$$

To effectively simulate and evaluate the GLINT processing techniques, GRB light curve data containing assemblages of time-tagged photons were acquired from several existing missions. As time-tagging of incoming photons is performed with respect to mission-specific timescales, burst data were first time-standardized to seconds-of-day UT1. An example burst, GRB20110420A as observed by Swift and WIND, is shown in Fig. 4. This burst featured a fast rise in photon counts, as seen in the Swift/BAT light curve, displayed as a dotted line. The WIND observed profile, shown as a solid line, produced a corresponding energetic spike 1.863 s later,

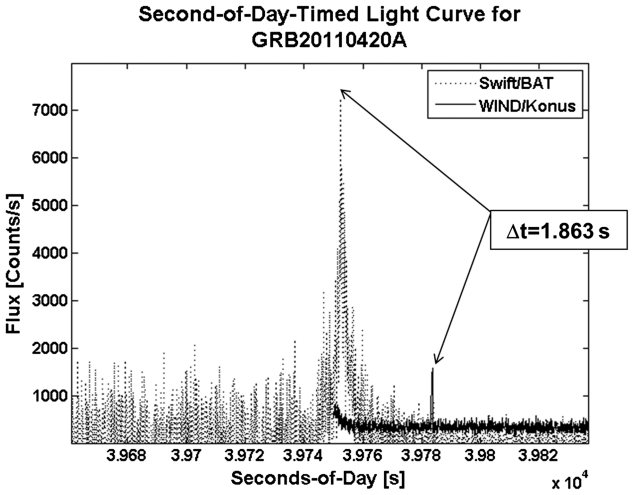

Fig. 4 GRB20110420A, a FRED-type burst yielding accurate TDOA values.

according to the difference in times of the profile peaks. Differences in the magnitude of flux between the peaks observed by Swift and WIND are due to differences in detector energy ranges. This TDOA measurement between profiles represents the delay of the arrival of the burst between the Swift and WIND vehicles, as Swift is in a high Earth orbit, and WIND is at the Earth–Sun L1 Lagrange point. Based upon the known spacecraft locations at the detection times of this burst's peak, the measured geometry-based offset along the LOS to the burst is 1.947 s. The difference between the known geometrical offset and the TDOA measurement is therefore 84 ms. Using Eq. (1), this geometrical-based time offset vs observed time offset discrepancy yields a position uncertainty of greater than 20,000 km. However, the limitation of the burst profile's bin size of 64 ms used by both Swift and WIND largely contributes to this computed uncertainty (~2 bins). Moreover, even with this potentially large uncertainty, this simple example based upon peak arrival time of binned photon data effectively demonstrates the GLINT concept in principle. To demonstrate the GLINT concept with improved capabilities, refined cross-correlation methods with the ability to attain time uncertainties less than 1 ms with existing GRB observation data are further described next.

VII. Methods of GRB Comparison

To support the evaluation of existing GRB data for TDOA measurements in navigation, multiple methods of comparing and time-aligning GRB light curves have been devised. These methods, described in further detail next, include a maximum burst peak alignment, a MATLAB cross-correlation function, and a Fourier domain burst phase alignment.

A GLINT burst TDOA analysis tool was created to process binned light curve data from multiple sets of two specified spacecraft. Once time-standardized light curves from the preprocessed photon data are generated, an Earth-centered inertial (ECI) LOS is calculated for the detected GRB event to the spacecraft using its right ascension and declination values provided by GCN's burst alert notices. To validate the TDOA value between spacecraft for each burst, the tool referenced the spacecraft position at the time of peak emission. To do this, it read in the spacecraft ephemeris data and located the spacecraft position at the peak time in the light curve, using a piecewise cubic hermite interpolation of spacecraft ephemeris data to find the position at the peak time. Figure 5 shows the GRB pulse alignment from two observing vehicles, first by aligning the pulse peak according to the detector trigger time noted in the GCN alerts and then by a second-of-day timing, according to the actual photon-measured arrival time at the vehicle.

A. Maximum Burst Peak Alignment

A simple burst comparison method used, as illustrated for GRB20110420A in Fig. 4, compares the burst peak arrival times. The

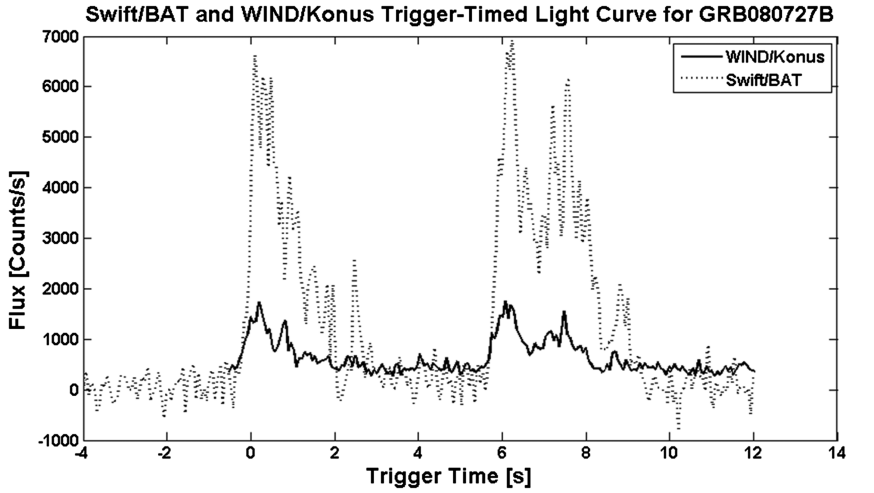

a)

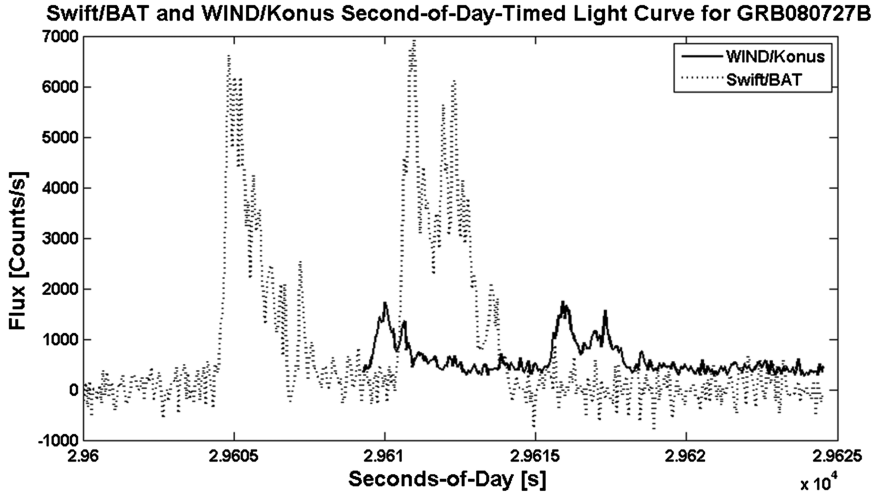

b)

Fig. 5 Comparisons using two GRB instruments for GRB080727B, using a) trigger time and b) second-of-day.

light curve profiles for a selected burst, as seen by two or more spacecraft are overlaid according to their binned, time-stamped data. The exact second-of-day time of the observed maximum intensity value corresponding to the burst peak is recorded. The TDOA measurement is the difference of these burst peak times between vehicles. Broader GRBs that lack the fast rise burst in Fig. 5 are not as easily compared by peak alignment. However, the rapid increase in flux at the initial burst emission lends itself to the multiple sharp maxima for this burst, resulting in accurate TDOA determination.

B. Burst Profile Cross Correlation

To improve upon the performance of the GRB profile time alignment and use all the burst's photon data, TDOA determinations for the GRBs using a cross correlation of the light curves were accomplished using MATLAB's built-in xcorr function. This function uses two burst profiles as input, and its output of the cross correlation lags indicates the individual bin offset between burst profiles.

C. Fast Fourier Transform Fitting

A Fourier domain cross-correlation analysis of GRB profiles was accomplished using the fast Fourier transform fit (FFTFIT) algorithm [24], to produce a more refined TDOA result than the two preceding techniques. This FFTFIT technique and software tool has been previously developed for radio and x-ray pulsar timing analysis; a recent implementation is part of the overall PSRCHIVE software package [25]. This tool estimates fractions of a bin offset, or lags, between two light curves without attempting to derive an arrival time of the peak for each. As FFTFIT resolves TDOA lags as a small fraction of a time bin for bursts that have desired profile characteristics for good processing candidacy, TDOA resolutions are improved using FFTFIT over both peak alignment and cross-correlation methods described previously. Many of the TDOA lags computed by FFTFIT were on the order of one-hundredth of a bin, yielding accuracies less than a millisecond using bin sizes for analyzed observations ranging from 32 to 64 ms. The benefit of the FFTFIT processing tool is the ability to correlate bursts with broader morphological profiles than the previous two methods.

D. GRB Time Offset Computation Results

Data from existing spacecraft and instruments were investigated, including both Earth-orbiting and deep-space vehicles. These instruments included the BAT onboard Swift, Konus onboard WIND, the anticoincidence shield of the spectrometer (SPI-ACS) onboard INTEGRAL, the wide area monitor (WAM) of Suzaku, MESSENGER's gamma-ray neutron spectrometer (GRNS), and Mars Odyssey's high-energy neutron detector (HEND). Photon fluxes measured by the instruments onboard most spacecraft have been stored in timed bins, with the bin size varying between instruments. TDOA measurements demonstrated agreement between multiple methods including maximum burst peak, burst cross correlation, and FFTFIT. The measured TDOA from each method and the actual known vehicle geometry-based time offset were compared to compute the number of bins of accuracy achievable.

Most GRB events, including GRB20080727B shown in Fig. 5, featured distinct periods of emission, which could be easily correlated with the corresponding energetic spike seen by another spacecraft for which methods such as maximum burst peak can work well. Precise TDOA calculations for bursts displaying chaotic and noisy structures, for instance, GRB20080319B, are more difficult to achieve using the maximum burst peak method, lacking well-defined features to isolate. The same holds true for bursts exhibiting plateau profiles with long and broad features on the time axis.

Using the known spacecraft geometry, an analysis of the xcorr cross-correlation technique indicates equally good or better results as the maximum burst peak method. In many cases where the burst does indeed display morphologies of sharp peaks or distinct, well-separated features (e.g., GRB20080727B) the peak time alignment method results are slightly better than cross correlation, as the latter method attempts to align the entire temporal profile of the burst, much of which can contain noise that distorts the light curve. However, in cases where the GRB profile lacks a defined feature like a sharp peak (e.g., GRB20080319B) cross correlation using xcorr of the light curves yields an improved TDOA, with uncertainties of two time bins or less. Accurate alignment using peak time estimates is ineffective using these types of bursts, as their profiles can be too broad and chaotic for isolating and windowing individual time-specific features.

For a preliminary GLINT concept analysis, several dozen representative GRB-spacecraft pairings were analyzed using the preceding three TDOA comparison techniques. All bin offsets for processed TDOA calculations were within four bins of accuracy, with many measurements within a fraction of a bin of precision representing uncertainties of 1 ms or less. As anticipated, bursts with sharp, energetic peaks and short durations are found to yield the most accurate TDOA comparisons. A small sample of nine processed bursts is provided in Table 1.

Limitations on TDOA bin resolution have been shown to depend largely on current photon data formats and binning sizes. Most GRB detector mission bin sizes are between 32 and 64 ms. Through advances in timing and data storage capabilities, this bin timing is expected to be capable of improvement to 1 ms-bins. The Konus instrument onboard WIND is currently capable of 2 ms-bin resolution for some triggered bursts [26]. Further advancement is likely, with the recent progress of technologies such as the Jet Propulsion Laboratory Deep Space Atomic Clock (DSAC), capable of subnanosecond time uncertainties [27]. Current GRB processing using FFTFIT has achieved one-one hundredth of a bin uncertainty ranges. For enhanced performance, GLINT would require planned improvements to data processing techniques and significantly enhanced γ-ray detector timing capabilities to achieve binning of less than 100 μs, such that burst TDOA uncertainties of 1 μs or less would be achievable.

VIII. GLINT Navigation Algorithms

To further evaluate the performance of the designed GLINT concept, two navigation algorithm methods were devised that use simulated GRB TDOA measurements as input. The first approach produces a single scalar value that is computed using the TDOA measurement to formulate range between vehicles along the LOS to the GRB, as in Eq. (1). The second approach formulates a full three-axis relative position measurement based upon Eq. (1), and is expected to provide an improved approach over the scalar method.

The primary function of the GLINT navigation system is to determine the accurate, full, 3-D position, expressed as $r = r_{SC} = \{r_x, r_y, r_z\}^T$, and velocity $v = v_{RSC} = \{v_x, v_y, v_z\}^T$ of the remote spacecraft. These navigation states can be with respect to an inertial origin or expressed relative to a base, or reference, spacecraft located at r_{Base}. The position separation, or difference, Δr, between these vehicles is computed as

$$\Delta r = r_2 - r_1 = r_{SC} - r_{Base} \tag{2}$$

The diagram in Fig. 3 shows this relationship and how the time offset relates to the position separation expressed in Eq. (2). The primary measurement of the GLINT navigation system is the time offset of the GRB arrival between two spatially separated spacecraft. The time offset, Δt, is computed as accurately as possible by any of the GRB comparison methods described previously.

To provide optimal GLINT data processing, the observations of the GRB time offsets can be processed with an extended Kalman filter (EKF) [28]. The GLINT EKF uses the high-fidelity orbit dynamics of a vehicle, processes measurements, and updates the error solution and covariances. Between burst measurements, the motion of the vehicles is incrementally propagated forward. The EKF designed for GLINT uses the filter states of the error of position and velocity of the remote vehicle. Error estimates of spacecraft clock synchronization, GRB direction, and planetary ephemeris could be included as state variables in future implementations of the GLINT EKF. The EKF dynamics and processing flow are shown in Fig. 6.

The navigation states of the GLINT navigation system and EKF follow the methods previously developed for the XNAV system [4,6,8]. The EKF states, $\boldsymbol{x}$, are vehicle position, r, and velocity, v, as $x = [\, r \quad v \,]^T$. The nonlinear spacecraft orbital dynamics can be expressed as

$$\dot{x}(t) = \boldsymbol{f}(x(t), t) + \boldsymbol{\eta}(t) \tag{3}$$

In Eq. (3), $\boldsymbol{f}$ is the nonlinear state vector function, as $\boldsymbol{f}(x(t), t) = [\, \dot{r} \quad \dot{v} \,]^T = [\, v \quad a \,]^T$ where a is the vehicle acceleration. The second term in Eq. (3), $\eta(t)$, is the noise vector associated with the unmodeled state dynamics. Using the dynamic models of acceleration of the spacecraft, including the primary orbiting body gravitational effects and higher-order disturbances, the full vehicle state dynamics can be expressed [6].

The GLINT Kalman filter is an EKF due to the nonlinear dynamics of the orbiting spacecraft. The states of the GLINT EKF are the errors of the state vector. These error states, $\delta \boldsymbol{x}$, can be represented based upon the true states, $\boldsymbol{x}$, and the estimated states, $\tilde{\boldsymbol{x}}$, as

$$\boldsymbol{x} = \tilde{\boldsymbol{x}} + \delta \boldsymbol{x} \tag{4}$$

Following the past navigation filter derivations, the full GLINT EKF error state dynamics and state covariances for the remote spacecraft can be propagated in time [4,6,8].

Table 1 GLINT timing resolution capabilities

GRB identifier	Spacecraft observer 1[a]	Spacecraft observer 2[a]	Max peak alignment resolution, s	Burst profile cross correlation resolution, s	FFTFIT resolution, s	FFTFIT uncertainty, s
20100625A	Sw	*I*	0.033	0.053	0.002	———
20100625A	Sz	*W*	0.019	0.005	———	———
20100625A	Sz	*I*	0.046	0.044	0.007	———
20101219A	W	Sw	0.012	0.012	0.012	0.003
20111113A	W	*I*	0.128	0.128	0.006	0.001
20111121A	Sz	Sw	0.003	———[b]	———	———
20111121A	W	Sw	0.017	0.017	0.013	0.002
20111121A	W	Sz	0.003	0.003	———	———
20120324	W	Sw	0.041	0.128	0.063	0.012

[a]Sw = Swift/BAT; Sz = Suzaku/WAM; *W* = WIND/Konus; *I* = INTEGRAL/SPI-ACS.
[b]Calculation not possible due to issues stated in text.

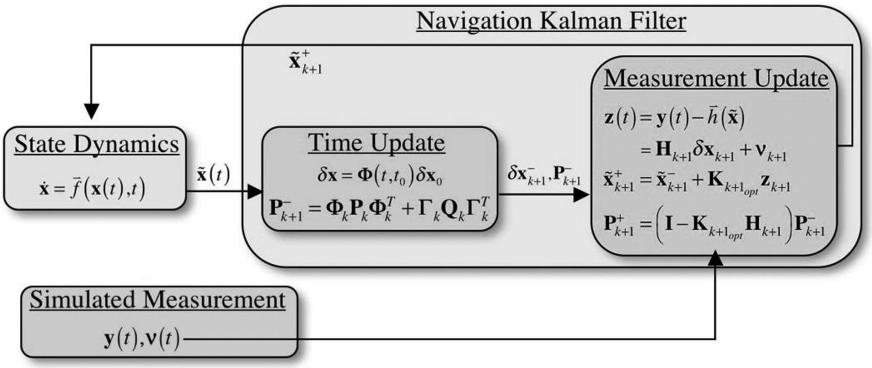

Fig. 6 Kalman filter dynamics and measurement processing data flow.

The GLINT observations, $\boldsymbol{y}$, follow a relationship with respect to the states as

$$y(t) = \boldsymbol{h}(x(t), t) + \boldsymbol{v}(t) \tag{5}$$

In this expression, $\boldsymbol{h}$ is a nonlinear function of the state vector, and perhaps time. The measurement noise associated with each observation is represented as $\boldsymbol{\nu}$.

To assemble the GLINT observation in terms of the error states of the EKF, the measurement difference, $\boldsymbol{z}$, is computed as

$$\begin{aligned} z(t) &= y(t) - \boldsymbol{h}(\tilde{\boldsymbol{x}}) = \frac{\partial \boldsymbol{h}(\tilde{\boldsymbol{x}})}{\partial \boldsymbol{x}}\delta\boldsymbol{x} + \boldsymbol{v}(t) \\ &= H(\tilde{\boldsymbol{x}})\delta\boldsymbol{x} + \boldsymbol{v}(t) \end{aligned} \tag{6}$$

This measurement difference, $z(t)$, is referred to as the *measurement residual*, and H is the *measurement matrix* of measurement partial derivatives with respect to the states [28].

Based upon the diagram in Fig. 3, a scalar measurement implementation follows from the range calculation using the observed GRB time offset as

$$\begin{aligned} z(t) &= c\Delta t - \hat{\boldsymbol{n}}^T\Delta r \\ &= [\,\hat{\boldsymbol{n}}^T \quad 0_{1\times 3}\,]\delta\boldsymbol{x} + v(t) \end{aligned} \tag{7}$$

This scalar method is straightforward to calculate from the GRB time offset, Δt, and the estimated remote spacecraft position and known base spacecraft position, Δr. Any discrepancy computed in z is related to the errors in the remote spacecraft position and velocity using Eq. (7). The range measurement is a singular scalar value and can only adjust a portion of the estimated vehicle position and velocity with each GRB observation.

A second measurement approach uses a full 3-D approach in order to correctly adjust all three axes of position and velocity with each GRB observation. This vector measurement method is devised as

$$\begin{aligned} z(t) &= (c\Delta t)\hat{\boldsymbol{n}} - (\hat{\boldsymbol{n}}^T\Delta r)\hat{\boldsymbol{n}} \\ &= [(\hat{\boldsymbol{n}}\cdot\hat{i})\hat{\boldsymbol{n}}^T\ 0_{1\times 3};\ (\hat{\boldsymbol{n}}\cdot\hat{j})\hat{\boldsymbol{n}}^T\ 0_{1\times 3};\ (\hat{\boldsymbol{n}}\cdot\hat{k})\hat{\boldsymbol{n}}^T\ 0_{1\times 3}]\delta\boldsymbol{x} + \boldsymbol{\nu}(t) \end{aligned} \tag{8}$$

where $\{i, j, k\}$ are the unit axis directions for the spacecraft's coordinate system.

IX. GLINT Navigation Simulation and Performance

A simulation, written in MATLAB, was developed to evaluate the performance of the GLINT navigation algorithms. The simulation propagates a truth model of a spacecraft on an interplanetary trajectory, and compares a similar trajectory initially injected with position and velocity errors that is continually corrected by GLINT measurements. The comparison of the truth trajectory with the corrected simulation provides an evaluation of EKF performance.

To evaluate the benefits of the GLINT navigation system, comparisons to DSN navigation solutions were produced. This approach is similar to past research on the evaluation of navigation using x-ray pulsars [8]. A simulated heliocentric trajectory was chosen as 100 days prior to a rendezvous at Mars, which was implemented based upon available trajectory data for the Mars Science Laboratory (MSL) vehicle. [For a comparison of detector size to previously stated missions, MSL's radiation assessment detector (RAD) weighs 1.56 kg and is roughly 240 cm^3 in volume [29].] The Earth-to-Mars interplanetary trajectory simulation used a numerical orbit propagator with 1000 s time steps acceptable for this cruise phase of the mission's trajectory. All third-body effects are considered, including eight planets, one dwarf planet, Earth's moon, and solar radiation pressure acting on the filter states. Initial errors in each axis for position and velocity of 100 m and 0.1 m/s, respectively, were used to simulate a significant drift from truth of a navigation solution. The EKF's initial covariance estimates were selected as $\sigma_{\text{pos}_0} = 500$ m and $\sigma_{\text{vel}_0} = 0.5$ m/s, primarily to support the large initial errors present within the simulations.

Simulated measurements were created using the truth trajectory data while incorporating the appropriate system measurement model and its expected uncertainty. The measurement noise was varied for each measurement using its $1-\sigma$ uncertainty value and a multiplicative factor based upon a random number generator.

With its multi-axis observation per measurement, the GLINT EKF vector method, as expected, consistently provided improved processing and performance over the single-axis scalar method. Therefore, the simulation's EKF measurement options reported here to evaluate the GLINT performance include three primary test scenarios: 1) DSN's ΔDOR (differential one-way ranging) only; 2) GLINT vector only; and 3) GLINT vector + DSNns range only. The various measurement uncertainty and frequency were varied for different sets of simulation runs. DSN ΔDOR measurement uncertainty was selected to be the stated 1 nrad capability of the system, processed once per day [30]. DSN range-only observations used a radial-only measurement accuracy of 1 m with observation frequency varied between once per day to once per 30 days. Uncertainties of the GLINT vector measurements were modeled based upon a burst TDOA performance from 10.0 μs down to 0.1 μs, with observation frequencies between one and four every two days. Only those measurements that passed an innovations test were processed in the EKF.

GRB measurements were simulated using random sky locations for the bursts. This randomness of the location is accurate based upon past GRB all-sky observations. A Monte Carlo analysis was performed, with 15 simulated runs with different random number seeds per run to generate the simulated navigation system measurements. The results of the full Monte Carlo output were then averaged to produce a resulting performance value for that set of runs.

An example simulation output of the covariance and state error plots is shown in Fig. 7, which provides a $1-\sigma$ covariance boundary of each position axis as well as truth minus simulation error throughout the run. The 3-D inertial $\{x, y, z\}$ position axes plots have been converted to Earth-to-remote-spacecraft radial, along-track, and

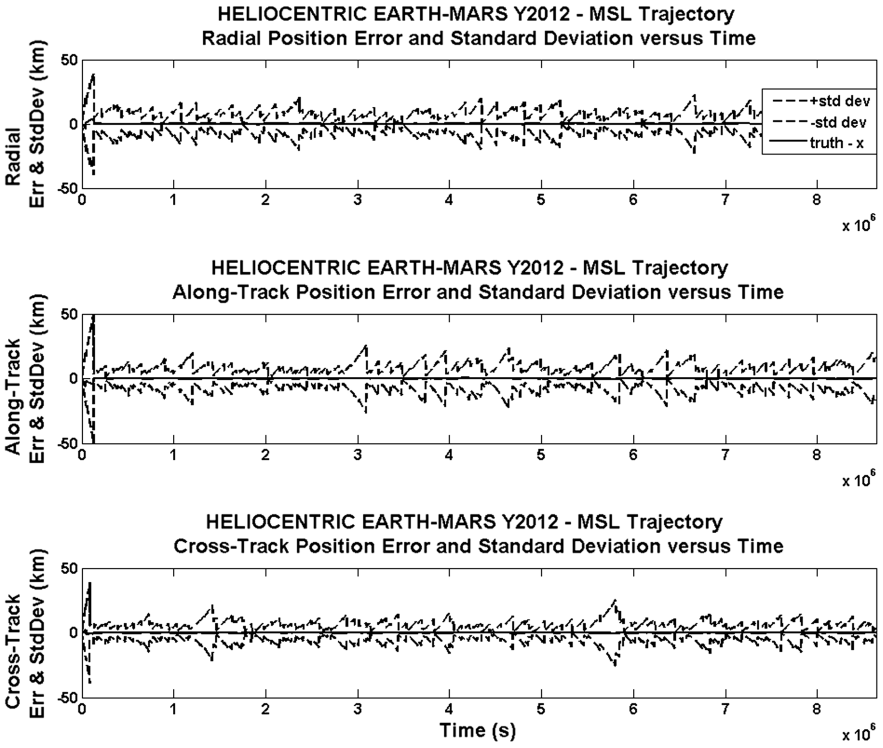

Fig. 7 EKF covariance envelope plots for simulated Mars rendezvous. The state error is also shown from the entire run, and remains within the envelope.

cross-track error plots. As shown in Fig. 7, starting with the stated initial errors in position, errors grow quickly over time until measurements begin to be processed, where eventually, with sufficient measurements, the initial position errors are essentially removed.

The averaged results from the Monte Carlo simulation runs are provided in Tables 2–4. The first rows of the EKF simulation in Table 2 show results based upon DSN's 1 nrad ΔDOR measurement accuracy [30]. The errors in this case on a 100-day run are very low on the radial component, but larger along-track and cross-track errors remain (following a general rule of 1 km per astronomical unit position error growth for DSN). Covariance estimates for DSN ΔDOR observations are fairly low, but the values shown in Table 2 are highly driven by process noise, dependent on the dynamics model validity.

The other two rows in Table 2 represent a vector GLINT measurement with uncertainty of 10 and 1 μs, respectively. These values were chosen to represent a one and two order of magnitude improvement over what is achievable today. Although the 1 μs TDOA uncertainty shows better results, both these sets of runs show that the GLINT vector measurement method is capable of approaching DSN's accuracy. Moreover, because the GRBs are geometrically separated and detectors are capable of making measurements along the LOS to each of the sources, the DSN-related issue of errors building up in the along-track and cross-track axes does not exist for GLINT. The GLINT covariance estimates are much larger, which was an expected result, as this method only makes a limited number of measurements each day contributing to all three axes.

Table 3 provides simulation results in which GLINT would augment DSN operation, lending itself to its full operational concept, so as not to compete with DSN, but rather be a supplemental improvement. DSN range-only measurements taken once every 30 days augmented with GLINT measurements provide for reduced operational costs (ΔDOR measurement, which can require more complex operations). GLINT measurement accuracies in the first two rows of Table 3 were set at 10 μs. Although errors in all three axes remain larger than with ΔDOR, reducing DSN range measurements from 10 to 30 days shows no significant loss in accuracy. The third and fourth rows represent an increased GLINT accuracy of 1 μs. In

Table 2 EKF example simulation performance for DSN and GLINT

		After 3 days			After 30 days		
EKF	Error type	*R*	*A*	*C*	*R*	*A*	*C*
DSN ΔDOR	Pos rms error, m	69	978	1039	76	898	1179
	Cov mean, m	2925	3041	2946	2958	3049	2962
GLINT, 2 per day	Pos rms error, m	1585	1278	875	1575	1339	922
Vector, 10 μs	Cov mean, m	8458	8336	6436	8020	8543	6415
GLINT, 2 per day	Pos rms error, m	993	883	721	984	876	677
Vector, 1 μs	Cov mean, m	8373	8088	5926	8562	7803	5842

Table 3 EKF simulation results for GLINT + DSN measurements

		After 3 days			After 30 days		
EKF	Error type	*R*	*A*	*C*	*R*	*A*	*C*
GLINT (10 μs, 2 perday) + DSN Range (every 30 days)	Pos rms error, m	7628	7477	5764	7281	7501	5780
GLINT (10 μs, 2 perday) + DSN Range (every 30 days)	Cov mean, m	11926	12366	8992	11801	12713	8941
GLINT (10 μs, 2 perday) + DSN Range (every 10 days)	Pos rms error, m	6576	7799	5496	6735	7795	5607
GLINT (10 μs, 2 perday) + DSN Range (every 10 days)	Cov mean, m	10942	11396	8607	10861	10576	8684
GLINT (1 μs, 2 perday) + DSN Range (every 30 days)	Pos rms error, m	1124	1178	976	944	1229	1030
GLINT (1 μs, 2 perday) + DSN Range (every 30 days)	Cov mean, m	8494	8585	6443	8097	8460	6724
GLINT (1 μs, 2 perday) + DSN Range (every 10 days)	Pos rms error, m	1114	1103	875	1229	1214	893
GLINT (1 μs, 2 perday) + DSN Range (every 10 days)	Cov mean, m	7005	7538	6256	7572	7708	6207

Table 4 EKF simulation results for high-accuracy GLINT + DSN measurements

EKF	Error type	After 3 days			After 30 days		
		R	*A*	*C*	*R*	*A*	*C*
GLINT vector only (0.1 μs, 2 per day)	Pos rms error, m	135	136	106	128	137	108
GLINT vector only (0.1 μs, 2 per day)	Cov mean, m	8831	8455	6500	8742	8694	6475
GLINT (0.1 μs, 2 perday) + DSN Range (every 30 days)	Pos rms error, m	134	138	101	129	140	102
GLINT (0.1 μs, 2 perday) + DSN Range (every 30 days)	Cov mean, m	8909	8412	6498	8838	8642	6457
GLINT (0.1 μs, 2 perday) + DSN Range (every 1 day)	Pos rms error, m	38	149	113	38	147	112
GLINT (0.1 μs, 2 perday) + DSN Range (every 1 day)	Cov mean, m	2556	5334	4123	2562	5602	4018

this case, whereas radial errors are larger compared to ΔDOR levels, along-track and cross-track errors are driven down to the order of ΔDOR uncertainties. The covariance estimate is large due to the fewer number of measurements overall. Based on the spacecraft EKF simulation results, capabilities of reducing along-track and cross-track errors for future DSN missions are anticipated. GLINT measurement accuracies at the 1 μs level will require implementation of planned improvements to detector photon timing and data-binning techniques.

With current day bin sizes on the order of tens of milliseconds and TDOA uncertainties determined to be one-one hundredth of a bin, if future γ-ray detector bin sizes of less than 1 ms are achieved, then TDOA measurement uncertainties may be several orders of magnitude improved over today's capabilities. Therefore, Table 4 represents a simulation in which GLINT augments DSN range-only operation with a highly-optimistic measurement uncertainty for GLINT of 0.1 μs. Results in this case are very comparable to DSN overall. As shown, if DSN range measurements are taken once every 30 days augmented with GLINT, providing for reduced operational costs, this approach alone yields very close measurements to DSN ΔDOR capabilities.

The results of this analysis show that:

1) As anticipated, successively finer time resolution of the GRB TDOAs improved the GLINT-based solutions.

2) GLINT-based solutions were capable of reducing all axes of position and velocity errors, whereas DSN measurements primarily reduced the radial direction error values.

3) The DSN range-only solutions could be reduced from once per day to once per 30 days without significant degradation of the navigation solution when augmented with GLINT measurements.

4) The GLINT observations could achieve subkilometer errors if GRB TDOA accuracies of less than 1 μs could be achieved.

X. Conclusions

The results of the GLINT concept analysis establish the feasibility and innovation of a novel relative navigation technique using GRB TDOA measurements. Specifically, this GLINT evaluation demonstrated the ability to use existing GRB TDOA data to compute spacecraft-range measurements that match measured spacecraft geometries. Using an interplanetary navigation simulation, it was shown that anticipated GLINT performance could achieve positional accuracies on the order of current DSN capabilities. Additionally, the augmentation of GLINT measurements allows DSN contact frequency with spacecraft to be reduced, freeing up valuable NASA resources for additional exploration missions. GLINT has been shown to be very complementary to the DSN, and is supported by the likelihood that all upcoming deep-space missions will continue to be equipped with onboard γ-ray detectors. Additionally, the current infrastructures of the IPN and GCN and their supporting spacecraft provide for an existing system for observing and communicating GRB localizations for GLINT implementation. It has been demonstrated that photon timing and processing capabilities at the submicrosecond level facilitates viable full implementation of this concept, with the potential to significantly enhance deep-space autonomous navigation capabilities.

Acknowledgments

This work was conducted and supported under NASA Small Business Innovative Research contract NNX12CE15P. The authors thank the following for their contribution toward this GLINT concept and research. Kevin Hurley of the Space Sciences Laboratory at the University of California, Berkeley, and Scott Barthelmy of the NASA Goddard Space Flight Center for their discussions on the IPN and GCN systems, and their assistance in obtaining γ-ray mission data, including Mercury MESSENGER data. Koji Mukai of the Suzaku (United States) Guest Observer Facility and the members of the Suzaku (Japan) science team, specifically Madoka Kawaharada, for their assistance in obtaining and using mission-specific ephemeris data. Adam Szabo of the Heliospheric Physics Laboratory (NASA Goddard Space Flight Center) for his help in WIND mission orbit data retrieval. Keith Gendreau of NASA Goddard Space Flight Center for his significant concept discussions. Charles Naudet of NASA's Jet Propulsion Laboratory for providing trajectory data for Mars Science Laboratory. Richard Schirato of the Los Alamos National Laboratory and John Goldsten of the Johns Hopkins University Applied Physics Laboratory for their useful discussions of GRB detection, especially in Earth orbit. John Gaebler of the NASA Goddard Space Flight Center who served as our contract technical representative. The GLINT development team, including Zaven Arzoumanian, John Hanson of CrossTrac Engineering, Inc., and Paul Graven of Cateni, Inc.

References

[1] Mudgway, D. J., *Uplink-Downlink, A History of the Deep Space Network 1957-1997*, NASA, Washington, D.C., 2001, Chaps. 8–9. doi:10.1086/386502

[2] Thornton, C. L., and Border, J. S., *Radiometric Tracking Techniques for Deep Space Navigation*, Wiley, Hoboken, NJ, 2003, Chap. 5. doi:10.1002/0471728454

[3] Hanson, J. E., "Principles of X-Ray Navigation," Ph.D. Dissertation, Stanford Univ., Stanford, CA, 1996. doi:10.2172/877425

[4] Sheikh, S. I., "The Use of Variable Celestial X-Ray Sources for Spacecraft Navigation," Ph.D. Dissertation, Univ. of Maryland, College Park, MD, 2005.

[5] Sheikh, S. I., Pines, D. J., Wood, K. S., Ray, P. S., Lovellette, M. N., and Wolff, M. T., "Spacecraft Navigation Using X-Ray Pulsars," *Journal of Guidance, Control, and Dynamics*, Vol. 29, No. 1, 2006, pp. 49–63. doi:10.2514/1.13331

[6] Sheikh, S. I., and Pines, D. J., "Recursive Estimation of Spacecraft Position and Velocity Using X-Ray Pulsar Time of Arrival Measurements," *Navigation: Journal of the Institute of Navigation*, Vol. 53, No. 3, 2006, pp. 149–166. doi:10.1002/j.2161-4296.2006.tb00380.x

[7] Golshan, A. R., and Sheikh, S. I., "On Pulse Phase Estimation and Tracking of Variable Celestial X-Ray Sources," *Proceedings of the 63rd Annual Meeting of the Institute of Navigation*, Institute of Navigation, Cambridge, MA, April 2007, pp. 413–422.

[8] Sheikh, S. I., Hanson, J. E., Collins, J., and Graven, P. H., "Deep Space Navigation Augmentation Using Variable Celestial X-Ray Sources," *Proceedings of the National Technical Meeting*, Institute of Navigation, Anaheim, CA, Jan. 2009, pp. 34–48.

[9] Sheikh, S. I., Hanson, J. E., Graven, P. H., and Pines, D. J., "Spacecraft Navigation and Timing Using X-Ray Pulsars," *Navigation: Journal of the Institute of Navigation*, Vol. 58, No. 2, 2011, pp. 165–186. doi:10.1002/j.2161-4296.2011.tb01799.x

[10] Ostlie, D. A., and Carroll, B. W., *Introduction to Modern Stellar Astrophysics*, Addison Wesley Longman, Reading, MA, 2006, pp. 545–550.

[11] Fenimore, E. E., and Galassi, M., "Gamma-Ray Bursts: 30 Years of Discovery: Gamma-Ray Burst Symposium," *American Institute of*

Physics Conference Proceedings 727, American Institute of Physics, Melville, NY, 2004, pp. 312–315.
[12] Sari, R., "Gamma-Ray Bursts: 5th Huntsville Symposium," *American Institute of Physics Conference Proceedings 526*, edited by Kippen, R. M., Mallozzi, R. M., Fishman, G. J., and Connaughton, V., American Institute of Physics, Melville, NY, Oct. 2000, pp. 504–513.
[13] Klebesadel, R., Strong, I. B., and Olson, R. A., "Observations of Gamma-Ray Bursts of Cosmic Origin," *The Astrophysical Journal*, Vol. 182, June 1973, pp. L85–L88.
doi:10.1086/181225
[14] Sazonov, S. Y., Lutovinov, A. A, and Sunyaev, R. A., "An Apparently Normal Gamma-Ray Burst with an Unusually Low Luminosity," *Nature*, Vol. 430, 2004, pp. 646–648.
doi:10.1038/nature02748
[15] Abdo, A. A., et al., "The First FERMI Large Area Telescope Catalog of Gamma-Ray Pulsars," *The Astrophysical Journal Supplement Series*, Vol. 187, No. 2, 2010, pp. 460–494.
[16] Quilligan, F., McBreen, B., Hanlon, L., McBreen, S., Hurley, K. J., and Watson, D., "Temporal Properties of Gamma Ray Bursts as Signatures of Jets From the Central Engine," *Astronomy and Astrophysics*, Vol. 385, No. 2, 2002, pp. 377–398.
doi:10.1051/0004-6361:20020038
[17] Bhat, P. N., Briggs, M. S., Connaughton, V., Kouveliotou, C., Horst, A. J., Paciesas, W., Meegan, C. A., Bissaldi, E., Burgess, M., Chaplin, V., Diehl, R., Fishman, G., Fitzpatrick, G., Foley, S., Gibby, M., Giles, M. M., Goldstein, A., Greiner, J., Gruber, D., Guiriec, S., Kienlin, A. V., Kippen, M., McBreen, S., Preece, R., Rau, A., Tierney, D., and Wilson-Hodge, C., "Temporal Deconvolution Study of Long and Short Gamma-Ray Burst Light Curves," *The Astrophysical Journal*, Vol. 744, No. 2, 2011, pp. 141–179.
doi:10.1088/0004-637x/744/2/141
[18] MacLachlan, G. A., Shenoy, A., Sonbas, E., Dhuga, K. S., Cobb, B. E., Ukwatta, T. N., Morris, D. C., Eskandarian, A., Maximon, L. C., and Parke, W. C., "Minimum Variability Time Scales of Long and Short GRBs," *Monthly Notices of the Royal Astronomical Society*, Vol. 432, No. 2, 2013, pp. 857–865.
doi:10.1093/mnras/stt241
[19] Hakkila, J., and Preece, R. D., "Unification of Pulses in Long and Short Gamma-Ray Bursts: Evidence from Pulse Properties and their Correlations," *The Astrophysical Journal*, Vol. 740, No. 2, 2011, p. 104.
doi:10.1088/0004-637x/740/2/104
[20] Zhang, F. W., Shao, L., Yan, J. Z., and Wei, D. M., "Revisiting the Long/Short-Short/Hard Classification of Gamma-Ray Bursts in the Fermi Era," *The Astrophysical Journal*, Vol. 750, No. 2, 2012, p. 88.
doi:10.1088/0004-637x/750/2/88
[21] Stamatikos, M., Sakamoto, T., and Band, D. L., "Correlative Spectral Analysis of Gamma-Ray Bursts Using Swift-BAT and GLAST-GBM," *American Institute of Physics Conference Proceedings*, Vol. 1065, No. 1, 2008, pp. 59–62.
doi:10.1063/1.3027959
[22] Nolan, P. L., et al., "Fermi Large Area Telescope Second Source Catalog," *The Astrophysical Journal Supplement*, Vol. 199, No. 2, 2012, p. 46.
[23] Hurley, K., Briggs, M. S., Kippen, R. M., Kouveliotou, C., Fishman, G., Meegan, C., Cline, T., Trombka, J., McClanahan, T., Boynton, W., Starr, R., McNutt, R., and Boër, M., "The Interplanetary Network Supplement to the Burst and Transient Source Experiment 5B Catalog of Cosmic Gamma-Ray Bursts," *The Astrophysical Journal Supplement Series*, Vol. 196, No. 1, 2011, pp. 1–15.
doi:10.1088/0067-0049/196/1/1
[24] Taylor, J. H., "Pulsar Timing and Relativistic Gravity," *Philosophical Transactions: Physical Sciences and Engineering*, Vol. 341, No. 1660, pp. 117–134.
doi:10.1098/rsta.1992.0088
[25] van Straten, W., Demorest, P., and Oslowski, S., "Pulsar Data Analysis with PSRCHIVE," *Astronomical Research and Technology*, Vol. 9, No. 3, 2012, pp. 237–256.
[26] Aptekar, R. L., Cline, T. L., Frederiks, D. D., Golenetskii, S. V., Mazets, E. P., and Pal'shin, V. D., "Konus-Wind Observations of the New Soft Gamma-Ray Repeater SGR 0501 + 4516," *The Astrophysical Journal*, Vol. 698, No. 2, 2009, pp. 82–85.
doi:10.1088/0004-637x/698/2/l82
[27] Tjoelker, R. L., Burt, E. A., Chung, S., Hamell, R. L., Prestage, J. D., Tucker, B., Cash, P., and Lutwak, R., "Mercury Atomic Frequency Standard Development for Space Based Navigation and Timekeeping," *43rd Annual Precise Time and Time Interval (PTTI) Systems and Applications Meeting Proceedings*, Institute of Navigation, Long Beach, CA, Nov. 2001, pp. 293–304.
[28] Gelb, A. (ed.), *Applied Optimal Estimation*, MIT Press, Cambridge, MA, 1974, pp. 182–203.
[29] Hassler, D. M., et al., "The Radiation Assessment Detector (RAD) Investigation," *Space Science Review*, Vol. 170, Nos. 1–4, 2012, pp. 503–558.
doi:10.1007/s11214-012-9913-1
[30] Lanyi, G., Bagri, D. S., and Border, J. S., "Angular Position Determination by Spacecraft by Radio Interferometry," *Proceedings of the IEEE*, Vol. 95, No. 11, Nov. 2007.
doi:10.1109/jproc.2007.905183

C. D'Souza
Associate Editor